DEUTSCHES ELEKTRONEN-SYNCHROTRON

DESY 97-016
February 1997

Deep Inelastic Physics at HERA

G. Ingelman

Deutsches Elektronen-Synchrotron DESY, Hamburg

and

Dept. of Radiation Sciences, Uppsala University, Sweden

ISSN 0418-9833

NOTKESTRASSE 85 - 22607 HAMBURG

To be sure that your preprints are promptly included in the
HIGH ENERGY PHYSICS INDEX,
send them to (if possible by air mail):

DESY **Bibliothek** **Notkestraße 85** **22607 Hamburg** **Germany**	**DESY-IfH** **Bibliothek** **Platanenallee 6** **15738 Zeuthen** **Germany**

DESY 97-016
February 1997

ISSN 0418-9833

Deep Inelastic Physics at HERA[1]

G. Ingelman

Deutsches Elektronen-Synchrotron DESY, Notkestrasse 85, D-22603 Hamburg, FRG
Dept. of Radiation Sciences, Uppsala University, Box 535, S-751 21 Uppsala, Sweden

Abstract: Electron-proton collisions in HERA provide a rich field of fundamental physics — proton structure, electroweak and strong interactions as well as new physics beyond the standard model. A review is given on a selection of main issues of current interest: electroweak interactions at high Q^2, densities and QCD dynamics of small-x partons in the proton, multiple gluon emission and effects on the hadronic final state, the transition from hard perturbative to soft non-perturbative QCD, rapidity gap events and their interpretation based on pomeron exchange or alternative models with novel soft colour interactions.

1 HERA collider and kinematics

HERA at DESY collides 27.6 GeV electrons or positrons on 820 GeV protons giving a cms energy $\sqrt{s} \simeq 300\,GeV$. This is an order-of-magnitude higher than achieved in fixed target experiments, which would need a lepton beam of $50\,TeV$ (!) to reach the same cms energy. The higher energy at HERA gives access to new kinematic domains and physics phenomena.

The observable process is $e+p \to \ell+H$, with the respective four-vectors p_e, p_p, p_ℓ, p_H. The scattered lepton, ℓ, is an electron or neutrino in case of neutral or charged current interaction mediated by an exchanged γ/Z^0 or W, respectively, that carries a momentum transfer $Q^2 = -q^2 = -(p_e - p_\ell)^2$. The hadronic final state H has an invariant mass W given by $W^2 = p_H^2 = (q+P)^2 = Q^2(1-x)/x + m_p^2$. It is often convenient to use the dimensionless scaling variables Bjorken-$x = Q^2/2P\cdot q$ and $y = P\cdot q/P\cdot p_e$ in the range $[0,1]$. For the overall event kinematics only two of these variables are independent and hence by measuring, e.g., the energy and angle of the scattered lepton all others can be calculated. For theoretical purposes, cross section formulae etc, the variables (x,y) or (x,Q^2) are usually used as the independent ones.

The accessible x and Q^2 region at HERA is shown in Fig. 1, illustrating the orders-of-magnitude increased range compared to fixed target experiments. The higher Q^2 provides a better resolution limit, $d[cm] \approx 2\cdot 10^{-14}/\sqrt{Q^2}[GeV]$, such that smaller structures can be explored. This continues the important rôle of lepton-nucleon scattering for our understanding of the internal structure of the nucleon. The size of the proton was first measured by electron scattering at Stanford in the mid 50's [1] and its composite, 'grainy' structure discovered with the SLAC 21 GeV electron beam in 1968/69 [2]. Together with the later muon and neutrino beam experiments at CERN and Fermilab [3], this confirmed the quark-parton model (QPM) [4] of the proton. HERA will thus investigate the proton structure with higher resolution. The extension to smaller x also opens new windows to QCD dynamics, as will be discussed in following sections.

[1]Invited talk at the 20th Johns Hopkins workshop, Heidelberg 1996

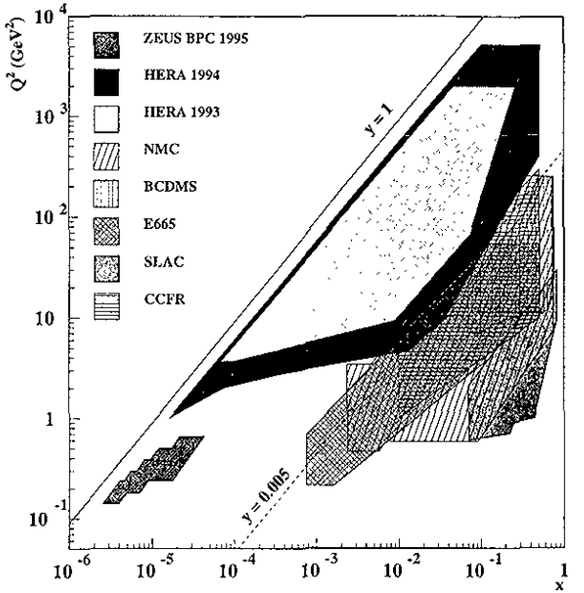

Figure 1: Accessible x, Q^2 region at HERA in comparison with fixed target experiments.

Due to the large imbalance of the electron and proton beam momenta in HERA, the ep cms is moving with $\beta = 0.93$. The phase space is therefore quite elongated in the 'forward' proton beam direction [5] such that the events are asymmetric with most of the final state hadrons in the 'forward' region. Therefore the detectors have a corresponding asymmetric design, see Fig. 2 which also shows a typical event with the scattered electron balanced by a jet of hadrons plus additional more forward hadrons, although the most forward ones are lost in the beam pipe.

In these general considerations no assumption is made about the structure of the proton and the origin of the final hadronic state. In the quark-parton model the current couples to a quark. By *assuming* the quark four-vector to be $p_i = \xi(E_p, 0, 0, E_p)$ and the initial and final quark to be massless one finds $\xi = x$, such that x is the momentum fraction carried by the struck quark in the proton. However, this relation and interpretation is modified when QCD corrections, giving virtual masses and transverse momenta, are taken into account [6]. The hadronic final state arises from the hadronization of a parton system composed of the scattered quark, the proton remnant and any additional emitted partons.

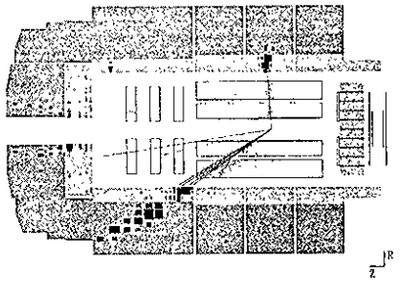

Figure 2: Cut along the beam axis of the H1 detector (length $\sim 8m$), with central and forward trackers surrounded by electromagnetic and hadronic calorimeters. The outer parts (not shown) include the superconducting solenoid, the muon detectors and luminosity monitors. Neutral current event $ep \to eX$ ($Q^2 = 2470\,GeV^2$, $x = 0.13$) with the electron (coming from the left) scattered upwards and an opposite jet of hadrons from the scattered quark in the proton (coming from the right) and more forward particles from the proton remnant.

The data samples collected have increased steadily with HERA running in the past few years, see Fig. 3. Still, the integrated luminosity is not yet the desired one. This is not surprising since HERA is the first ep collider ever built and is a complex system, with two essentially independent accelerators (for e and p) plus a series of pre-accelerators. The specific luminosity (i.e. peak luminosity per colliding bunch and unit bunch current) is actually almost twice as large as the design value and the proton beam life time is very good. However, the electron beam life time is too short due to interactions with ions produced from remaining gas or dust particles. A positron beam, on the other hand, repels the positively charged particles from the circulating beam resulting in an acceptable beam life time. Therefore, positrons have been used since July 1994 to obtain higher luminosity (increased slope in Fig. 3).

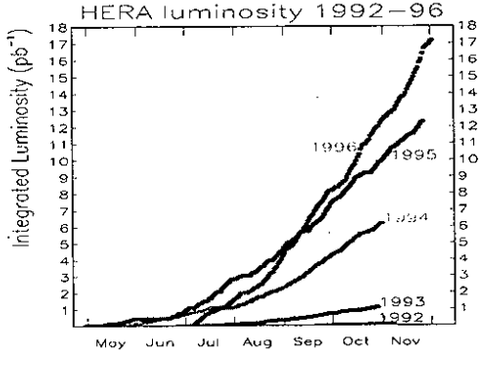

Figure 3: Yearly integrated luminosity in HERA running.

The reliability of this complex machine is, however, still not good enough and a consolidation program is carried out to increase it. Thus, HERA has delivered 17 pb^{-1} in 1996 and one expects about 35 pb^{-1} per year thereafter. Still higher luminosity requires a machine upgrade, which has also been investigated within the workshop 'Future Physics at HERA' [9]. A decision on such an upgrade, with new beam focusing magnets close to the interaction points, will soon be taken and installation is planned for the winter shutdown 1999/2000. This should give luminosities of about 170 pb^{-1}/yr aiming at a total integrated luminosity of about 1 pb^{-1}.

HERA has therefore a substantial physics potential. Electroweak interactions can be investigated to large Q^2 and provide precision tests of the electroweak theory (section 2) as well as to search for new particles or interactions beyond the standard model. The proton structure can be further explored in terms of partons and QCD dynamics (section 3). At the highest Q^2 signs of quark or electron substructure may be observed or new bounds on their sizes be obtained. At low Q^2 the transition from deep inelastic scattering (DIS) to photoproduction ($Q^2 \simeq 0$) can be investigated and improve our understanding of hard versus soft physics (section 4). Photoproduction is also a rich field where HERA has already contributed many results. The hadronic final state provides additional observables to investigate QCD in both the perturbative and non-perturbative regions (section 5). A main current issue is the interpretation of the observed rapidity gap events (section 6). In the following, some of these topics will be discussed. The whole physics scope of HERA is simply too large to be covered in this review, which instead concentrates on these indicated topical issues of current HERA data analysis.

2 Electroweak cross-sections and propagator effects

The neutral current (NC) process, $e^{\mp}p \to e^{\mp}X$, has a differential cross section which in leading order theory is given by

$$\frac{d^2\sigma_{NC}(e^{\mp})}{dx\,dQ^2} = \frac{4\pi\alpha^2}{xQ^4}\left[y^2xF_1 + (1-y)F_2 \pm \left(y - \frac{y^2}{2}\right)xF_3\right] \quad (1)$$

$$= \frac{4\pi\alpha^2}{xQ^4}\left[\left(1 - y + \frac{y^2}{2}\frac{1}{1+R}\right)F_2 \pm \left(y - \frac{y^2}{2}\right)xF_3\right] \quad (2)$$

in terms of the nucleon structure functions $F_i(x,Q^2)$. The ratio $R = F_L/(F_2 - F_L)$, with $F_L = F_2 - 2xF_1$ the longitudinal structure function, is zero to first approximation leaving only two independent structure functions. This is due to the Callan-Gross relation, $2xF_1 = F_2$, which holds for spin 1/2 quarks when neglecting masses, intrinsic transverse momenta and order α_s QCD effects. At small-x and large y, however, R and F_L may become noticeable (see Fig. 8a below).

The structure functions are in the standard model given by

$$F_2(x,q^2) = \sum_{q=u,d,s,c\ldots}\left[xq(x,Q^2) + x\bar{q}(x,Q^2)\right]A_q(Q^2) \quad (3)$$

$$xF_3(x,q^2) = \sum_{q=u,d,s,c\ldots}\left[xq(x,Q^2) - x\bar{q}(x,Q^2)\right]B_q(Q^2) \quad (4)$$

in terms of the quark (antiquark) density distributions $q(x,Q^2)$ ($\bar{q}$) in the proton. For unpolarized $e^{\mp}$ beam, the flavour dependent coefficients are

$$A_q(Q^2) = e_q^2 - 2e_q v_e v_q P_Z + (v_e^2 + a_e^2)(v_q^2 + a_q^2)P_Z^2 \quad (5)$$

$$B_q(Q^2) = -2e_q a_e a_q P_Z + 4v_e a_e v_q a_q P_Z^2 \quad (6)$$

With $f = e,q$ for any fundamental fermion, e_f is here the electric charge ($e_e = -1$), $v_f = (T_{3f} - 2e_f \sin^2\theta_W)/\sin 2\theta_W$ and $a_f = T_{3f}/\sin 2\theta_W$ are the NC vector and axial vector couplings expressed in terms of the third component of the weak isospin ($T_{3e} = -\frac{1}{2}$) and the Weinberg angle θ_W. $P_Z = Q^2/(Q^2 + M_Z^2)$ is the ratio of the Z and γ propagators. The pure γ exchange term (without P_Z in eq. (5)) dominates completely at low Q^2, but with increasing Q^2 first the γ/Z^0 interference term (linear in P_Z) and then the pure weak term (quadratic in P_Z) become important and finally dominate the cross section at large Q^2.

The leading order differential cross-section for the charged current (CC) process, $ep \to \nu X$, is given by

$$\frac{d^2\sigma_{CC}(e^{\mp}p)}{dx\,dQ^2} = \frac{\pi\alpha^2}{4\sin^4\theta_W\,(Q^2 + M_W^2)^2} \left\{ \begin{array}{l} (u+c) + (1-y)^2(\bar{d}+\bar{s}) \\ (\bar{u}+\bar{c}) + (1-y)^2(d+s) \end{array} \right. \quad (7)$$

for unpolarized electrons and positrons, respectively. The quark densities are here abreviated $u = u(x,Q^2)$ etc, and M_W is the W-boson mass. The overall normalization can also be expressed in terms of the Fermi coupling constant $G_F = \pi\alpha/(\sqrt{2}\sin^2\theta_W M_W^2)$.

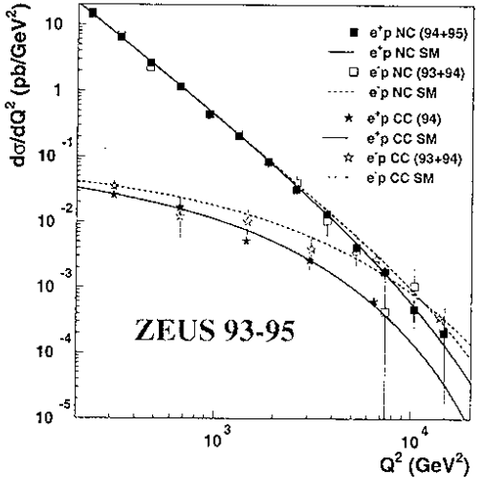

Figure 4: ZEUS data [10] on charged and neutral current cross-sections for $e^{\mp}p$ scattering compared to the electroweak standard model (curves) showing electroweak unification with the same magnitude of CC and NC cross-sections for $Q^2 \gtrsim M_{W,Z}^2$.

The NC and CC cross-sections have recently been measured by HERA up to large Q^2. As shown in Fig. 4, they agree very well with the predictions of the electroweak theory (i.e.

the above formulae with input quark density parametrizations). This confirms electroweak unification; in particular, the magnitude of the NC and CC cross-sections become similar at Q^2 around the weak boson masses.

Furthermore, using the shape and magnitude of the CC cross-section one can determine the propagator mass resulting in $m_W = 82^{+6}_{-5}(stat)^{+3}_{-3}(syst)\ GeV$ (preliminary) when combining H1 and ZEUS data [10]. Increased integrated luminosities will improve these measurements and facilitate others.

Polarized electron and positron beams provide an additional handle for precision tests of the standard electroweak theory, since the corresponding cross-section formulae [5] are modified. In particular, the coefficients in eq. (5,6) have another structure of electroweak vector and axial vector couplings. This provides more information that can be experimentally accessed, e.g. through various asymmetries [8, 9].

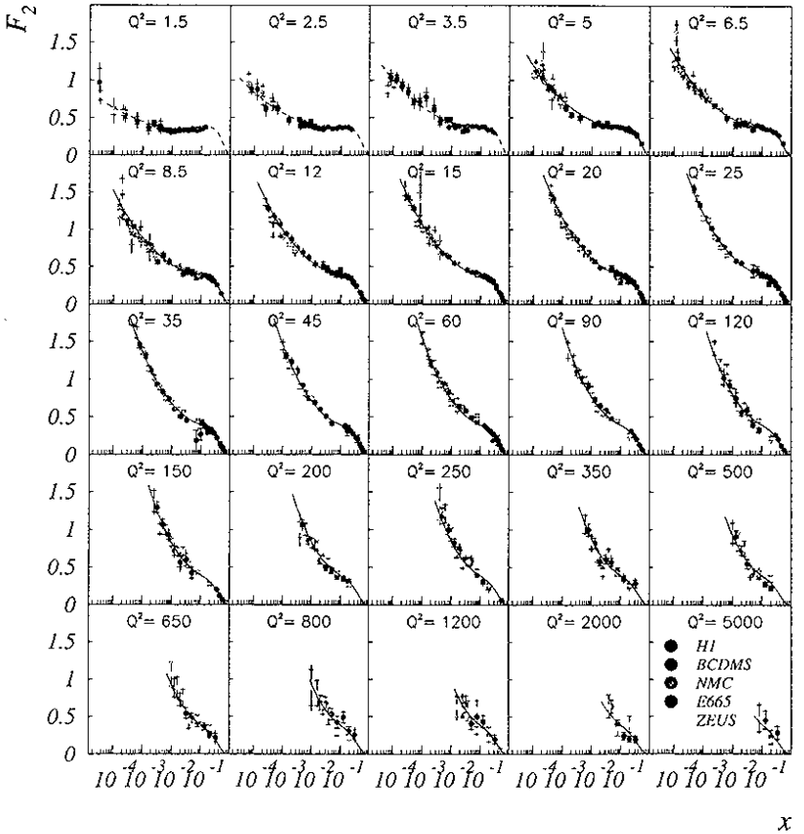

Figure 5: The proton structure function F_2 versus x for bins in Q^2. HERA data [11, 12] (H1, ZEUS) compared to fixed target data (BCDMS, NMC, E665).

3 Densities and dynamics of small-x partons in the proton

The basic experimental information on the parton content of the proton is given by the structure functions. $F_2(x, Q^2)$ can be extracted from the cross-section, eq. (2), where the small effects of R and xF_3 are either neglected or accounted for using theoretical expressions and parameterized parton densitites. The resulting HERA data [11, 12] on $F_2(x, Q^2)$, Fig. 5 and 6, show several important features. Most striking is the strong rise at small x, to be discussed in detail below.

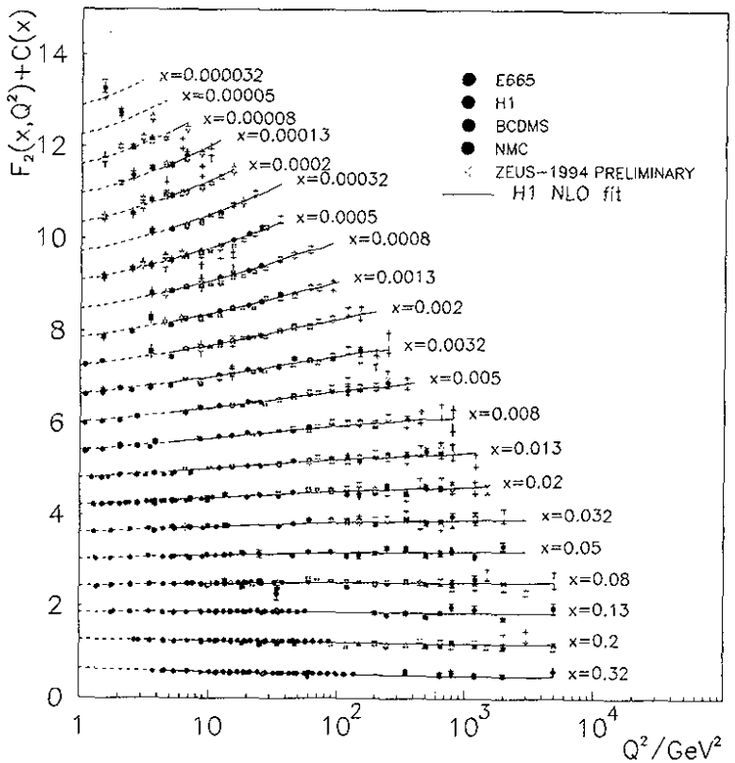

Figure 6: The proton structure function F_2 versus Q^2 for bins in x. HERA and fixed target data with fit (lines) to the QCD DGLAP evolution equations in next-to-leading-order.

The data from H1 and ZEUS agree well with each other. They also connect smoothly to the previous fixed target data and extend, as expected, to much smaller x and larger Q^2. With this large x, Q^2 range one observes very clear scaling violations, i.e. F_2 does not only depend on the dimensionless variable x but also on Q^2. As shown in Fig. 6, F_2 increases with Q^2 at small x and decreases with Q^2 at large x. Thus, at larger Q^2 there

are more softer partons (smaller momentum fractions x) and fewer hard ones. This results naturally from branching processes, such as $q \to qg$, $g \to q\bar{q}$ and $g \to gg$, in perturbative QCD (pQCD). The conventional Altarelli-Parisi equations [13] in next-to-leading order (NLO) give a good fit of the data over a very large region, $1.5 < Q^2 < 5000\, GeV^2$ and $3 \times 10^{-5} < x \lesssim 1$. In spite of this remarkable agreement, the proper interpretation of the rise of F_2 at small-x, and the corresponding parton dynamics, is a topical issue of research.

The basic physics of this behaviour of the structure function is that the quark being probed by the current (γ^*/Z^0) may have arisen through quantum fluctuations. In pQCD this can be represented by a ladder diagram as illustrated in Fig. 7a. The non-perturbative initial condition of the proton is defined in terms of parton densities ($q(x_0, Q_0^2)$, $g(x_0, Q_0^2)$) at the scale Q_0^2, giving the lower limit for perturbation theory to be applicable. Such an initial parton with momentum fraction x_0 may radiate partons in several steps, thus getting a successively smaller momentum fraction x_i but becoming off-shell with a space-like momentum ($p_i^2 < 0$). This virtuality, $Q_i^2 = -p_i^2$, is related to the transverse momentum $k_{i\perp}^2$ of the radiated partons, which are either on-shell or have a time-like virtuality ($p^2 > 0$) causing branches to on-shell partons. This evolution is a quantum fluctuation which can be made real if enough energy-momentum is provided by the electroweak probe such that the space-like quark at the top of the ladder can be turned into an outgoing on-shell or time-like quark. In the latter case, it will radiate additional partons to become on-shell.

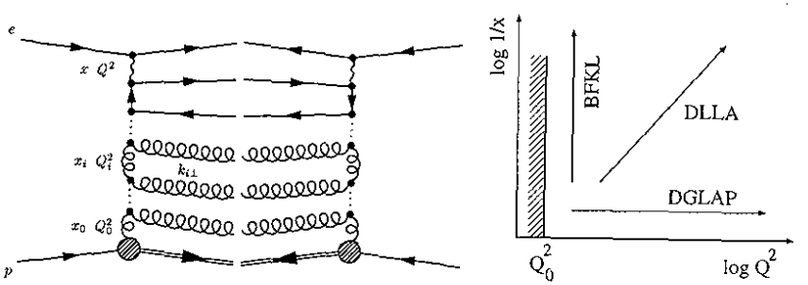

Figure 7: (a) QCD ladder diagram representing the squared amplitude, with a vertical cut representing the final state. (b) Applicability of approximation schemes in the x, Q^2 plane, with Q_0^2 giving the limit for pQCD.

The cross-section for this whole process should be calculated by squaring the diagram (Fig. 7), summing all possible emissions and integrating the momenta of emitted partons. The remaining degrees of freedom are x, Q^2 and the cross-section is essentially the quark density function $q(x, Q^2)$ at the weak boson vertex, cf. eq. (1). An exact calculation, with all interferences between different parton emissions, becomes extremely complicated and in practice not possible. It is therefore necessary to use approximations where the interferences are simplified or neglected. Different approximations are appropriate in different regions of phase space, as illustrated in Fig. 7b. These schemes and equations (often labelled with acronymes from the names of their originators) are here briefly discussed, refering to e.g. [14] for a more detailed account.

In conventional DIS with large Q^2 and not too small x, the dominant contributions are given by the Altarelli-Parisi or DGLAP equations [13]. The virtualities Q_i^2 in the ladder are here strongly ordered, i.e. $Q_0^2 \ll Q_1^2 \ldots \ll Q_i^2 \ll \ldots Q^2$, which is equivalent to the transverse momenta $k_{i\perp}^2$ being strongly ordered. The smallness of α_s is then compensated by a large $log\, Q^2$ such that $\alpha_s \log Q^2 \sim 1$ and terms involving $(\alpha_s \log Q^2)^n$ must therefore be summed to all orders in n to obtain the leading order (LO) result, i.e. the leading $\log Q^2$ approximation. In next-to-leading order (NLO) of DGLAP terms involving $\alpha_s^n \log^{(n-1)} Q^2$ are summed.

The approximation used in DGLAP is not appropriate at small enough x. If Q^2 is large and x is small, there will be large logarithms in both Q^2 and $1/x$ which must be resummed. When $\alpha_s \log Q^2 \log(1/x) \sim 1$, but $\alpha_s \log Q^2$ and $\alpha_s \log(1/x)$ are both small, the 'double leading log approximation' (DLLA) gives the dominant contribution by summing terms of $(\alpha_s \log Q^2 \log(1/x))^n$ to all orders in n. This corresponds to the case when not only the virtualities Q_i^2 in the ladder are strongly ordered, but also the momentum fractions x_i, i.e. $x \ll \ldots x_i \ll \ldots x_0$.

When x is small enough that $\alpha_s \log(1/x) \sim 1$, but $\alpha_s \log Q^2$ is small, the leading contribution is obtained by summing terms involving $(\alpha_s \log(1/x))^n$ giving the BFKL equation [15]. This means that the x_i are strongly ordered, but the virtualities or transverse momenta are not.

Theoretical research is presently trying to find a more general approximation scheme resulting in an equation that is applicable in these different regions. For example, the CCFM equation [16] gives BFKL at small-x and DGLAP at large x. The physics of these equations and their relation to data will now be discussed.

The Altarelli-Parisi (or DGLAP) equations express an evolution in $logQ^2$. They can be written in a matrix form

$$\frac{d}{d\log Q^2}\begin{pmatrix} q(x,Q^2) \\ g(x,Q^2) \end{pmatrix} = \begin{pmatrix} P_{qq} & P_{qg} \\ P_{gq} & P_{gg} \end{pmatrix} \otimes \begin{pmatrix} q \\ g \end{pmatrix} \tag{8}$$

which emphasizes that quark and gluon densities are coupled. The convolution, defined as $P_{ij} \otimes f_j = \int_x^1 dy/y P_{ij}(x/y) f_j(y,Q^2)$, express the possibility that a parton i with momentum fraction x may originate from the branching of a 'mother' parton j of higher momentum fraction y. The splitting functions $P_{i \leftarrow j} = \alpha_s P_{ij}^{(0)} + \alpha_s^2 P_{ij}^{(1)} + \ldots$ have been calculated to leading and next-to-leading order. The NLO DGLAP formalism can be fitted very well to the F_2 data as shown by the full lines in Fig. 6.

With this fit, which is mostly dominated by high statistics data at lower y, the contributon of F_2 to the cross-section at larger y can be calculated. Neglecting the small contribution from weak interactions, i.e. xF_3, the cross-section eq. (2) can be written

$$\frac{d^2\sigma}{dxdQ^2} = \frac{2\pi\alpha^2}{xQ^4}\left[(2-2y+y^2)F_2(x,Q^2) - y^2 F_L(x,Q^2)\right] \tag{9}$$

such that the longitudinal structure function F_L can be extracted at large y where its contribution is largest. The resulting first measurement [17] of F_L based on HERA data is shown in Fig. 8a. Its magnitude show the correctness of the treatment of R or F_L when extracting F_2 from eq. (2). Furthermore, the measured F_L is in good agreement with QCD, where in leading order

$$F_L(x,Q^2) = \frac{2\alpha_s}{\pi}x^2 \int_x^1 \frac{dy}{y^3}\left\{\frac{2}{3}F_2(y,Q^2) + \sum_q e_q^2\left(1-\frac{x}{y}\right) yg(y,Q^2)\right\} \tag{10}$$

The two terms originate from the QCD Compton process $\gamma^* q \rightarrow qg$ and boson-gluon fusion $\gamma^* g \rightarrow q\bar{q}$, where the latter dominates at small-x.

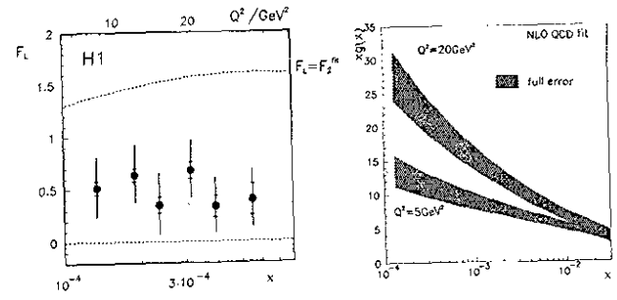

Figure 8: (a) The longitudinal structure function F_L as a function of x or Q^2 for $y = 0.7$. Data points from H1 [17] with statistical and full errors (statistical and systematic errors added in quadrature). The band represents F_L (with uncertainty) calculated in QCD using quark and gluon distribtions from data. (b) The gluon density $xg(x)$ (with error bands) at $Q^2 = 5$ and $20 GeV^2$ extracted from a NLO QCD fit to H1 data [11] of $F_2(x,Q^2)$.

Since the quark densities are coupled to the gluon density in the DGLAP equations, a fit of this formalism to F_2 data also gives a determination of the gluon density. The result [11] of the above NLO QCD fit is shown in Fig. 8b. It demonstrates the great improvement in our knowledge of the gluon density in the small-x region. With the much increased statistics in the 1994 data sample, the error bands are decreased such that measurements at different Q^2 can be clearly separated and the low-x limit pushed further down. With more statistics in coming years, the gluon density will become quite precisely measured in this new low-x region. Already with present data, one observes clearly the large and increasing gluon density at small-x (Fig. 8b). A simple parametrization is provided by [11] $xg(x, Q^2 = 5\, GeV^2) = 2.24\, x^{-0.20}\,(1-x)^{8.52}$.

The x-shape of the parton densities is not predicted by DGLAP, but must be obtained from data through a fit to some suitable form, e.g. [18] $xf_i(x) = A_i x^{-\lambda_i}(1-x)^{n_i}(1+\epsilon_i\sqrt{x}+\gamma_i x)$ with parameters for the different parton species $i = q, \bar{q}, g$. At small-x the structure function can therefore be fitted by $F_2 = \sum_{q\bar{q}} q(x) \simeq x^{-\lambda}$ and from HERA data at $x < 0.1$ one finds [11] that λ increases from about 0.2 at $1 < Q^2 < 10\, GeV^2$ to about 0.4 (large error bars) at $Q^2 < 10^2\, GeV^2$. This rise of F_2 at small x can be described in terms of DGLAP evolution in two different ways.

In the conventional case, such as in the MRS [18] and CTEQ [19] parametrizations of parton densities, the DGLAP evolution start at a scale $Q_0^2 \simeq 4\, GeV^2$ where pQCD should be safely applicable. The input sea quark and gluon distributions must then already be rising at small-x in order for the evolution to produce a fast enough rise in F_2. For example, one needs $xq_s(x,Q_0^2) \sim x^{-\lambda_s}$ and $xg(x,Q_0^2) \sim x^{-\lambda_g}$ with λ_s and λ_g around 0.2–0.3 depending on the details (evolution scheme, Q_0^2, other parameters). Nothing is really explained here since the problem is moved to understand why the input distributions rise at small-x.

In the other appoach, represented by the GRV parametrizations [20], the starting scale is as low as $Q_0^2 \simeq 0.3\,GeV^2$. This gives a long evolution range in $log\,Q^2$ such that the rise of F_2 can be obtained starting from distributions of valence quarks and 'valence-like' gluons, i.e. $xg(x,Q_0^2) \to 0$ when $x \to 0$. In these 'dynamical' parton densities the rise of F_2 is generated by conventional DGLAP evolution from simple parton densities at a starting scale which is unconventionally low and where pQCD may not be applicable. Nevertheless, this approach gives a very good description of the HERA F_2 data in Figs. 5 and 6. However, it fails to describe data at $Q^2 \lesssim 0.5\,GeV^2$ as demonstrated by the recent low-Q^2 data shown below in Fig. 10.

Fig. 8b shows the large density of gluons at small-x in the proton, e.g. $xg(x) = 10-30$ at $x = 10^{-4}$ depending on Q^2. It is substantially larger than F_2 in Fig. 5, which is essentially the sum of quark densities (modulo quark charges squared that sum to order unity). Thus, at small-x the proton is dominated by the gluons. The colour octet charge of the gluons makes them dominate the QCD evolution even more.

At small-x the ladder diagrams can therefore be approximated by having gluons only, plus a $q\bar{q}$ pair at the top where the electroweak boson couples (Fig. 7a). The dominant behaviour is then given by the gluon evolution

$$\frac{dxg(x,Q^2)}{d\log Q^2} \simeq x\int_x^1 \frac{dy}{y}\, g(y,Q^2)\, P_{gg} \simeq \frac{3\alpha_s}{\pi}\int_x^1 \frac{dy}{y}\, yg(y,Q^2) \tag{11}$$

where quarks have been neglected in the first step and only the singular part $P_{gg} \sim 6y/x$ of the splitting function has been kept in the last step. This corresponds to the double leading log approximation, with large $logQ^2$ and $log(1/x)$, giving a resulting gluon density

$$xg(x,Q^2) = xg(x,Q_0^2)\, exp\left\{2\sqrt{\frac{36}{25}\, ln\frac{ln(Q^2/\Lambda^2)}{ln(Q_0^2/\Lambda^2)}\, ln\frac{1}{x}}\right\} \tag{12}$$

where the exponential increases faster than any power of $ln(1/x)$, but slower than a power of $1/x$. Therefore, a singular input $xg(x,Q_0^2) \sim x^{-\lambda}$ would give the dominant small-x dependence. This gluon density will then give the main contribution to the small-x behaviour of the quark density at the top of the ladder and thereby of F_2.

The QCD evolution of F_2 in the limit of large Q^2 and small x can be reformulated [21] as a scaling in the variables

$$\sigma = \sqrt{\ln(x_0/x)\,\ln(t/t_0)}\,, \quad \rho = \sqrt{\frac{\ln(x_0/x)}{\ln(t/t_0)}} \tag{13}$$

where $t = \ln(Q^2/\Lambda^2)$. The 'double asymptotic scaling' of F_2 in these variables can then be demonstrated as follows. With R_F and R'_F calculable functions in QCD [21], the function $log(R'_F F_2)$ is asymptotically a linearly rising function with σ (at fixed large ρ), while $R_F F_2$ is asymptotically independent of ρ and σ. This holds as long as the parton densities at input for the evolution are not too singular. Singular boundary conditions, as in the BFKL behaviour $xg(x) \sim x^{-\lambda}$, would spoil this scaling. This predicted scaling behaviour is indeed observed [11] in the F_2 data for $Q^2 \gtrsim 5\,GeV^2$. This supports the conventional QCD evolution and sets limits on the BFKL contribution [21].

One can therefore conclude that the HERA F_2 data of present-day precision can be described by conventional QCD dynamics. However, this does not exclude that there

is some contribution of novel QCD dynamics at small-x. Thus, although the inclusive structure function measurements do not give any direct evidence for BFKL behaviour, it can also not yet be excluded.

The characteristic feature of BFKL dynamics is that the momentum fractions x_i are strongly ordered giving large logarithms in x that need to be resummed through terms of the type $(\alpha_s \log(1/x))^n$. However, the transverse momenta (or virtualities) in the ladder are not strongly ordered and can fluctuate along the ladder. One must therefore use the 'unintegrated' gluon density, which expresses the density of gluons of a certain virtuality k^2 and gives the ordinary gluon density when integrating over all virtualities

$$xg(x,Q^2) = \int^{Q^2} \frac{dk^2}{k^2}\, f(x,k^2) \tag{14}$$

The evolution of the gluon density is then given by the BFKL equation [15]

$$\frac{d\, f(x,k^2)}{d\, log(1/x)} = \int_{k_0^2} dk'^2\, K(k^2,k'^2) f(x,k'^2) \tag{15}$$

where the Lipatov kernel K is analogous to the Altarelli-Parisi splitting functions. The roles of virtualities k^2 and momentum fractions x are here interchanged compared to the DGLAP equations; the evolution is in $log(1/x)$ and the integration over virtualities. All virtualities are here possible, but a lower cut-off k_0^2 is needed to ensure the validity of the employed perturbation theory.

Solving the BFKL equation results in the x-behaviour of the gluon at small-x, where the approximation is valid, provided that an input gluon distribution in virtuality is given at some fixed x_0. The general result is that $f(x,k^2) \sim c \cdot x^{-\lambda}$, with the uncertainty from the non-perturbative cut-off k_0^2 mainly in the coefficient c. The expectation from BFKL dynamics is therefore $xg(x) \sim x^{-\lambda}$ where $\lambda = (3\alpha_s/\pi)4\ln 2 \approx 0.4 - 0.5$ for a fixed α_s. Taking into account the running of α_s and energy-momentum conservation, which is not explicitly included in this small-x approximation, tends to lower λ somewhat. This is quite compatible with the $x^{-\lambda}$ behaviour observed in F_2 and used as input in the parton density parameterizations used in the conventional QCD analyses above. Thus, BFKL dynamics could still play a role in the F_2 data, although there is no direct evidence for it.

It is, however, not yet clear that the structure function data do indeed rise as a power at small-x. In fact, an alternative is provided by a simple 'double-logarithmic scaling' function

$$F_2(x,Q^2) = a + b\log\frac{Q^2}{Q_0^2}\log\frac{x_0}{x} \tag{16}$$

which has been found [22] to describe the data well. Here, a, b and $x_0 = 0.074$, $Q_0^2 = 0.5\,GeV^2$ are parameters. This logarithmic scaling in both x and Q^2 corresponds to the first term in the DLLA scheme, i.e. $(\alpha_s \log Q^2 \log(1/x))^{n=1}$. Compared to BFKL's power dependence, $x^{-\lambda}$, this gives a less strong increase at small-x and avoids a potential problem with the unitarity limit as discussed in section 4.

A high gluon density at small-x corresponds to a kind of 'overcrowding' of the proton which will lead to interactions between these gluons. Thereby gluons may fuse or recombine, e.g. $gg \to g$, which will compensate the splitting process and reduce the increase in density. This novel dynamics is expected at small enough x. Correlations will result due to the merging of gluons from different fluctuations. In terms of pQCD diagrams, different

ladders will merge and give rise to fan-shaped ladder diagrams. These are summed in the GLR equation [23] which can be written in a simplified form [24]

$$\frac{d\,xg(x,Q^2)}{d\,logQ^2} = \frac{\alpha_s}{2\pi}x\int_x^1 \frac{dy}{y^2}P_{gg}\left(\frac{x}{y}\right)yg(y,Q^2) - \frac{81\alpha_s^2}{16Q^2R^2}\int\frac{dy}{y}\left[yg(y,Q^2)\right]^2 \qquad (17)$$

The first term is the normal DGLAP evolution (BFKL evolution would also be possible here) and the second term contains the new gluon recombination or 'screening' effect which lowers the gluon density due to its negative sign. The squared gluon density, which is an approximation for an unknown two-gluon correlation function, leads to novel non-linear effects in this small-x QCD dynamics. The $1/Q^2$ factor in the screening term reflects the higher twist nature of these diagrams where interactions between the partons occur. The dimension of this Q^2 factor is compensated by the parameter R^2 giving the size of the region of the interacting gluons. With R being simply the proton radius, the effect of the screening term is very small and hard to observe in the x, Q^2 region available at HERA [25]. However, the probability for interactions would be larger if the relevant size were smaller. This would be a kind of 'hot spots' in the proton, i.e. smaller regions with a higher than average gluon density [26]. These could be related to the valence quarks, but since nothing is really known this field is open for speculations. In any case, these are new and exciting possibilities in QCD at small-x when the proton is a new kind of many-body system!

4 The photon-proton cross-section

The increase of soft (small-x) partons observed in data and present in the QCD ladder schemes discussed above cannot continue without proper bounds. A too large parton density, i.e. structure function, would give a cross-section that is unphysically large and violates unitarity. The unitarity constraint is embodied in the Froissart bound [27] on total cross-sections, which can increase at most like $log^2 s$ in the limit of large cms energy $\sqrt{s}$.

It is therefore interesting to consider the photon-proton cross-section

$$\sigma^{\gamma^* p} \simeq \frac{4\pi^2\alpha}{Q^2}F_2(W^2,Q^2) \qquad (18)$$

as a function of its cms energy W. The available data are shown in Fig. 9 for different bins in Q^2, which is just another way of plotting the data in Figs. 5 and 6. Since $W^2 = Q^2(1-x)/x + m_p^2 \approx Q^2/x$ at small-x, the cross-section would increase as $\sigma \sim W^{2\lambda}$ if the parton densities increases as a power, i.e. $F_2 \sim x^{-\lambda}$. The full lines, which are the previously discussed fits of DGLAP evolution in QCD, have this behaviour. Thus, they illustrate a power behaviour of the cross-section, $\sigma \sim s^{\lambda}$, which will be in conflict with the Froissart bound when extrapolated to asymptotic energy. On the other hand, an increase of the structure function like $log(1/x)$, as in the double-logarithmic scaling discussed above, would be compatible with the unitarity limit.

This potential unitarity problem may find a solution in the above gluon recombination process, since an increasing gluon density gets reduced by the screening correction term in eq. (17) such that the cross-section is well-behaved.

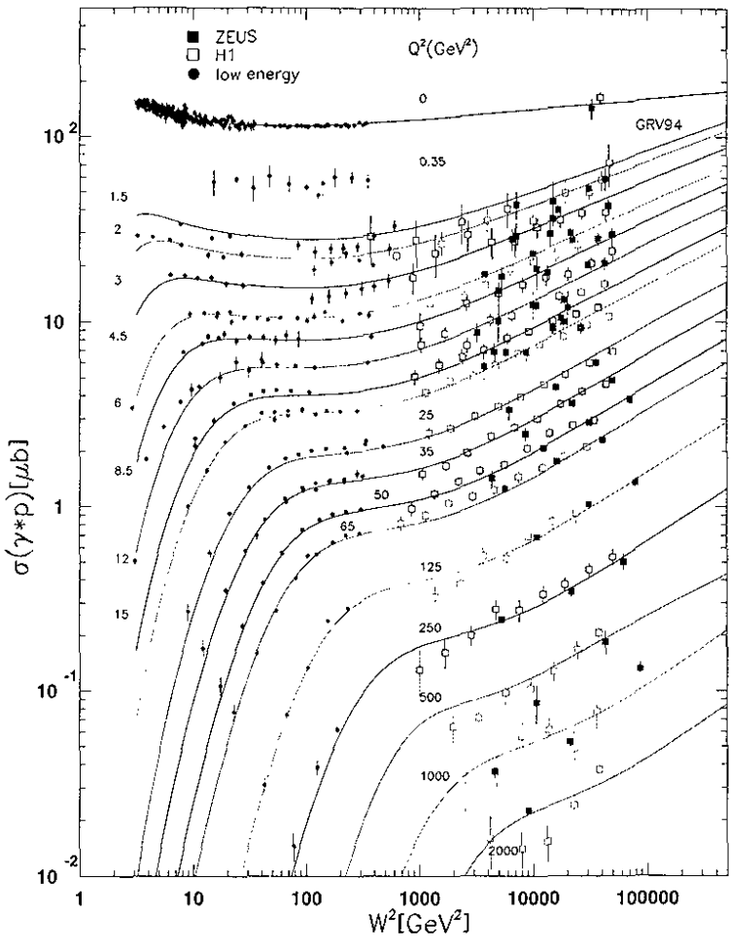

Figure 9: The photon-proton cross-section versus its cms energy W. HERA data from DIS at different Q^2, with QCD DGLAP fits (curves) as in Figs. 6, compared to photoproduction ($Q^2 \simeq 0$) at HERA and fixed target energies.

It is here also interesting to consider the transition from deep inelastic scattering to real photoproduction, i.e $Q^2 = 0$. The photoproduction cross-section data, also included in Fig. 9, show a less steep energy dependence. It can be fitted by $\sigma \sim W^{-2\lambda}$, where $\lambda \simeq 0.08$ rather than 0.2–0.4 as obtained in DIS. Thus, photoproduction has a slower rise with energy, as is characteristic for soft physics, whereas DIS has a faster rise characteristic for hard processes. The transition between these two regions is quite fast in Q^2. This is more clearly seen in Fig. 10, where the structure function $F_2(x)$ is shown for different Q^2 between 0.16 and 6.5 GeV^2. For $Q^2 \lesssim 1\ GeV^2$, the data are quite compatible with

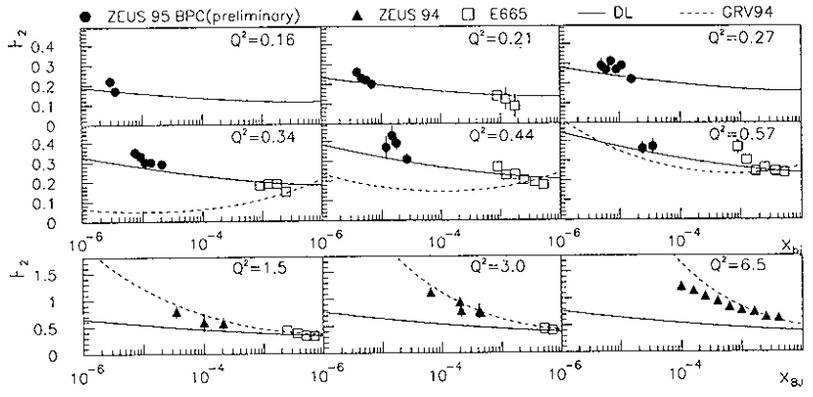

Figure 10: The proton structure function F_2 at small Q^2. Data from ZEUS [28] and fixed target (E665), compared to expectations from a Regge-based model [29] (DL, full curves) and the GRV [20] parton density evolution (dashed).

a Regge-based model [29] where the high energy behaviour of the cross-section is $s^{0.08}$ as obtained from fits to total cross-sections in hadronic interactions. This is characteristic for soft physics of Regge exchanges dominated by 'soft pomeron' exchange. For larger Q^2, however, this model is substantially below the data and cannot explain the rise of F_2 at small-x. This rise is therefore a significant new effect beyond soft physics and requires parton dynamics as discussed in section 3.

On the other hand, the hard physics in terms of pQCD evolution works at high Q^2. The 'hard pomeron' or BFKL ladder gives a steeper power rise $s^\lambda \sim x^{-\lambda}$ compatible with DIS data, but not needed to explain it. As discussed, DGLAP evolution is sufficient to describe the data well. Here, the GRV [20] formalism, which is the only one extendable to this low-Q^2 region, works down to $Q^2 \sim 0.5\,GeV^2$ but fails below, as seen in Fig. 10.

Thus, the photoproduction region and the DIS region are described by different theoretical approaches. The transition between them is not well understood and is a challenge for current research.

5 Parton emission effects on the final state

As seen in section 3, the data on the structure function is a too inclusive measurement to give decisive information on the presence of new QCD dynamics in the parton evolution. Although the data is consistent with expectations from BFKL behaviour, there is no need to include it since conventional DGLAP can describe the data well. However, the hadronic final state gives access to additional observables that provide more information. This may be used to discriminate between the different QCD schemes discussed above.

The flow of transverse energy ($E_\perp$) in the forward region has been extensively studied for this purpose. The main effects are here easily understood when considering the ladder

diagram in Fig. 7a. At small x more partons can be radiated before the original momentum fraction x_0 is degraded to x. Partons emitted in the lower part of the diagram (closer to the proton vertex) have larger momentum fractions and are therefore at more forward rapidities. Since the DGLAP evolution is strongly ordered in virtuality, the transverse momenta are more limited in the lower part of the diagram resulting in a suppressed $E_\perp$ flow at forward rapidities. On the other hand, BFKL has no such ordering in transverse momentum and therefore predicts a larger $E_\perp$ flow in the forward region.

The measured forward $E_\perp$ flow [30] is indeed larger than at first expected based on the Monte Carlo model LEPTO [31], including first order QCD matrix elements, higher order parton emissions based on DGLAP and hadronization using the Lund string model [32]. Estimates [33] based on the BFKL equation compares favourably with the data, but a detailed comparison cannot be made since a BFKL-based Monte Carlo model is lacking. However, the ARIADNE [34] Monte Carlo gives a good description of the data. It is based on the color dipole model (CDM) [35], which has some features that are similar to BFKL.

In the CDM, partons are radiated from colour dipoles ('antennas') that are formed by the coloured partons emerging from the hard scattering. In DIS, a quark-diquark may give a first dipole that radiate a gluon. This gives two dipoles, qg and $g(qq)$, which can radiate further giving an iterative process of new dipoles that radiate. Thus, the model is not based on Feynman diagrams as the above QCD evolution schemes. Therefore, it has no explicit dependence on x and Q^2. Instead, the essential quantity is the invariant mass of the dipole and the effective scale for the radiation in DIS is $W^{4/3}$. The emissions are ordered in transverse momentum, but not in rapidity. Therefore, when considering the emissions along the rapidity axis, the transverse momenta are not ordered but fluctuate. This is similar to BFKL behaviour and give more transverse energy at forward rapidities as compared to the DGLAP-based models. This is explicitly demonstrated in Fig. 11, which shows the density of emitted partons in the hadronic cms, i.e. photon-proton cms. The CDM model gives more transverse momentum emissions in the proton remnant side.

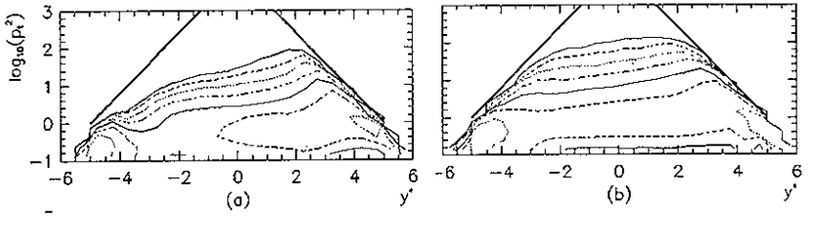

Figure 11: Density $dN/dy^* d\log_{10}(p_\perp^2)$ of emitted partons in the hadronic cms, with the proton remnant at $y^* < 0$, from (a) LEPTO and (b) ARIADNE for $x = 10^{-3}$, $Q^2 = 10 GeV^2$ at the HERA energy. The curves show constant density with a factor two between adjacent curves and the thick lines indicate the triangular phase space boundary.

However, the DGLAP-based LEPTO model can also describe the forward $E_\perp$ flow reasonably well, provided that some modifications are made in the non-perturbative parts of the model [36]. This concerns the treatment of the more complicated target remnants that arise when a sea quark interacted, leaving its partner anti-quark plus the valence

quarks in the remnant. Here, the left-over sea-quark partner may form an extra string together with another parton and thereby produce additional hadrons that contribute to the $E_\perp$ flow. This extra string also give better continuity in the model between non-perturbative sea quark interactions and perturbative $g \to q\bar{q}$ processes. The soft, non-perturbative colour interactions discussed in section 6, also contributes to an increased $E_\perp$ flow.

Thus, the global $E_\perp$ flow versus rapidity is still too inclusive to demonstrate a clear difference between parton emission in DGLAP and BFKL. Instead one should consider observables that are more directly sensitive to hard parton emissions and less influenced by soft hadronization effects. One such is the high-$p_\perp$ tail of the charged particle $p_\perp$ spectrum, which indeed show a difference at very small x between models based on DGLAP and the 'BFKL-like' CDM [37]. This is demonstrated in Fig. 12a, where the H1 data [38] are seen to favour CDM at the smallest x.

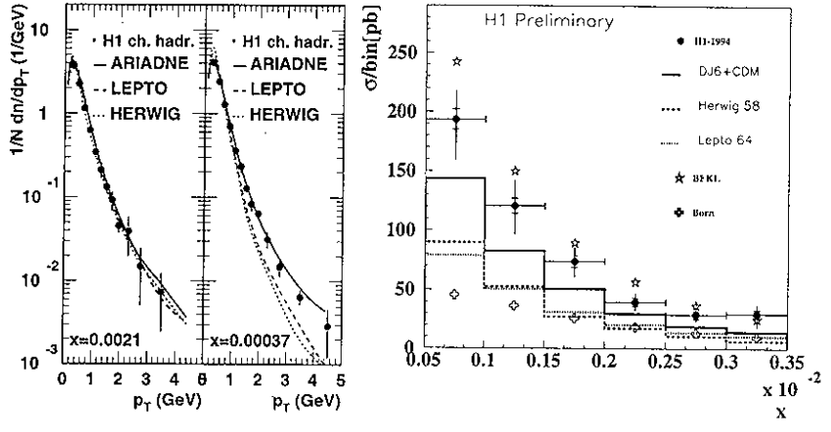

Figure 12: (a) Charged particle $p_\perp$ spectra in $0.5 < \eta < 1.5$ in the hadronic cms at $Q^2 \approx 14\,GeV^2$ for two x bins; H1 data [38] and Monte Carlo results from DGLAP-based models LEPTO, HERWIG and the CDM model ARIADNE. (b) Cross-section of forward jets versus x; H1 data [39] and QCD calculations based on Born graphs and on BFKL, and Monte Carlo models as in (a).

The standard way to access underlying hard parton emission processes is through jet reconstruction. The harder parton emissions in the forward region from BFKL should therefore be visible as an increased cross-section of forward jets. Recent HERA data [39] on forward jets ($7° < \theta_{jet} < 20°$, $E_{jet} > 28.7\,GeV$, $E_{\perp,jet} > 3.5\,GeV$) are shown in Fig. 12b. The increase at small-x is much stronger than expected from leading order matrix elements (Born) and the DGLAP-based Monte Carlos. The CDM-based Monte Carlo describes data much better, although it does not quite reproduce the strong increase at small-x. A genuine BFKL result is only available as parton level calculations [40] and agrees quite well with the data (perhaps increasing slightly too much), although a direct comparison cannot be made without taking hadronization effects into account. Thus, although additional work is needed here, this is presumably the strongest evidence for BFKL behaviour that exist at present.

6 Rapidity gap events

Much interest has been focused on the 'rapidity gap events' discovered at HERA [41, 42]. These are events with no particle or energy depositions in the forward part of the detector, i.e. the final state has a large gap in rapidity space. A typical such event is shown in Fig. 13a and demonstrates the striking difference compared to normal DIS events as examplified in Fig. 2. A simple observable to characterize the effect is η_{max} giving, in each event, the maximum pseudo-rapidity where an energy deposition is observed. (With $\eta = -\ln\tan\theta/2$ and θ the angle relative to the proton beam so that $\eta > 0$ is the proton hemisphere in the HERA lab frame.) Fig. 13b shows the distribution of this quantity based on ZEUS data [43].

Although the bulk of the data with η_{max} in the forward region is well described by ordinare DIS Monte Carlo events, there is a large excess with a smaller η_{max} corresponding to the central region or even in the electron hemisphere. The gap events have the same Q^2 dependence as normal DIS and are therefore not some higher twist correction. Their overall rate is about 10% of all events, so it is not a very rare phenomenon. Nevertheless, it came as a surprise to many, although the phenomenon had been predicted as an example of diffractive hard scattering [44].

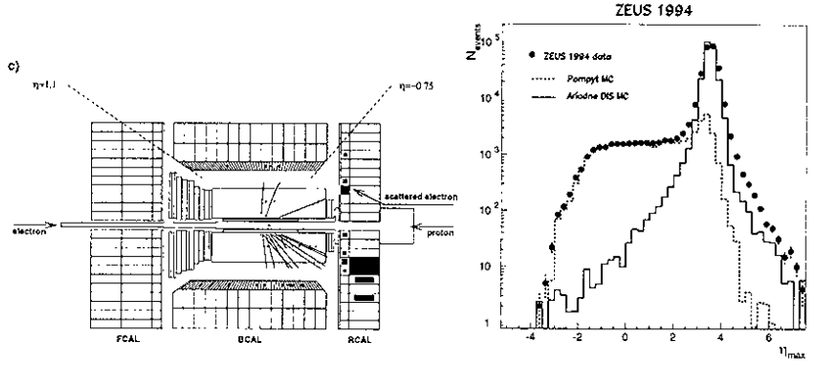

Figure 13: (a) The ZEUS detector with a rapidity gap event, i.e. having no particles or energy in the forward (proton beam direction) part of the detector. (b) Distribution of η_{max}, the maximum pseudorapidity of observed particles/energy, in ZEUS data compared to Monte Carlo simulations using ARIADNE [34] (full histogram) for ordinary DIS and POMPYT [53] (dashed) for DIS on a pomeron with a hard quark density ($zq(z) \sim z$), with normalisation adjusted such that the sum fits the data. Courtesy of the ZEUS collaboration [43].

In normal DIS, a quark is scattered from the proton leaving a colour charged remnant (diquark in the simplest case). This gives rise to a colour field (e.g. a string) between the separated colour charges, such that hadronization gives particles and energy flow in the whole intermediate phase space region as illustrated in Fig. 14a.

The, by now conventional, interpretation of the gap events is in terms of diffractive scattering. The deep inelastic scattering is then on an exchanged colour singlet object as illustrated in Fig. 14b. This gives no colour field between the hard scattering system and

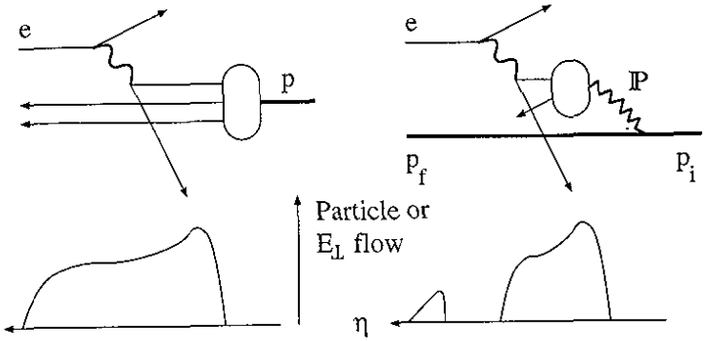

Figure 14: Illustration of (a) normal DIS and (b) diffractive DIS at HERA and the resulting particle or transverse energy flow in laboratory pseudorapidity.

the proton remnant system. Therefore, no hadrons are produced in the region between them, i.e. a 'rapidity gap' appears. The size of the gap is basically a kinematic effect. The larger fraction of the proton beam momentum that is carried by the forward going colour singlet proton remnant system, the smaller fraction remains for other particles which therefore emerge at smaller rapidity. The forward going system must also have a small invariant mass in order to escape undetected in the beam pipe. Thus, a favourable situation is when the incoming proton emerges with most of the momentum and only a very small angular deflection.

This corresponds to diffractive scattering in hadronic interactions, which is conventionally described using Regge phenomenology [45]. The dominant contribution is here given by the exchange of a pomeron ($\mathbb{P}$) carrying energy-momentum and vacuum quantum numbers. Although Regge phenomenology describes well the differential cross-sections for elastic and diffractive hadron-hadron scattering, it has not given a real understanding of the pomeron and its interaction mechanism. In a modern QCD-based language it is natural to consider the strongly interacting pomeron in terms of some partonic system. The old suggestion [46] that the pomeron is mainly composed of gluons has been a common assumption. Of course, it cannot be a real particle or state, since it has a negative mass square (t defined below). A natural thought is that the pomeron is a virtual glueball. This has some theoretical support since the Regge trajectory of glueballs, obtained from estimated glueball masses, has been claimed to coincide with that of the pomeron [47]. A recent glueball candidate [48] also fits on the pomeron trajectory. In a different approach [49], the pomeron is argued to have a pointlike coupling to quarks giving a dominant $q\bar{q}$ content of an effective parton structure.

If the pomeron has some parton content it should be possible to probe by hard scattering processes [44]. The UA8 experiment at the $Sp\bar{p}S$ collider has discovered [50] high-$p_\perp$ jets in high mass diffractive scattering that demonstrates an underlying parton level interaction. Furthermore, the data give evidence [51] for a component of 'superhard' partons in the pomeron, i.e. carrying essentially the whole pomeron momentum. The ideal way

to measure a parton structure of the pomeron is through deep inelastic scattering. As illustrated in Fig. 14b, the proton would here 'emit' a pomeron with a small squared momentum transfer $t = (p_i - p_f)^2$ and with a fraction $x_{I\!P} = 1 - x_p \lesssim 0.1$ of the initial proton momentum p_i ($x_p = p_f/p_i$). The pomeron is then probed by the electron as discribed by the usual DIS variables x and Q^2. The diffractive DIS cross-section can be written [52]

$$\frac{d\sigma(ep \to epX)}{dx\,dQ^2\,dx_{I\!P}\,dt} = \frac{4\pi\alpha}{xQ^4}\left[1 - y + \frac{y^2}{2}\right] F_2^D(x, Q^2; x_{I\!P}, t) \tag{19}$$

where the normal proton F_2 structure function has been replaced by a corresponding diffractive one, F_2^D, with $x_{I\!P}$ and t specifying the diffractive conditions. (For simplicity we here only consider the dominating electromagnetic interaction and neglect R.) Assuming Regge factorization of the pomeron vertices, F_2^D can be factorized into a flux of pomerons and a pomeron structure function, i.e. $F_2^D = f_{I\!P/p}(x_{I\!P}, t) \cdot F_2^{I\!P}(z, Q^2)$ where $z = x/x_{I\!P}$ is the momentum fraction of the parton in the pomeron.

The pomeron flux factor can be obtained from Regge phenomenology and, e.g., written in the form [49]

$$f_{I\!P/p}(x_{I\!P}, t) = \frac{9\beta_0^2}{4\pi^2}\left[F_1(t)\right]^2 \left(\frac{1}{x_{I\!P}}\right)^{2\alpha_{I\!P}(t)-1} \tag{20}$$

with parameters obtained from data on hadronic diffractive scattering. Here, $\beta = 3.24GeV^2$ and $F_1(t) = (4m_p^2 - At)/(4m_p^2 - t) \cdot (1 - t/B)^{-2}$ is a proton form factor with m_p the proton mass and parameters $A = 2.8$, $B = 0.7$. The pomeron Regge trajectory is

$$\alpha_{I\!P}(t) = 1 + \epsilon + \alpha' t \tag{21}$$

with $\epsilon \approx 0.08$ and the slope $\alpha' = 0.25$.

With an assumed parton content, the pomeron structure function is

$$F_2^{I\!P}(z, Q^2) = \sum_f e_f^2 \left\{ z q_f(z, Q^2) + z\bar{q}_f(z, Q^2) \right\} \tag{22}$$

in terms of densities of (anti)quarks of flavour f. Since DIS does not couple directly to gluons, they will only enter indirectly via $q\bar{q}$ pairs. The pomeron parton densities are unknown and must be chosen so as to reproduce data as well as possible.

This framework of diffractive hard scattering have been implemented in Monte Carlo event generators, e.g. POMPYT [53] and RAPGAP [54]. With suitable pomeron parton densities the salient features of the data can be well described. For example, with a hard quark component in the pomeron the η_{max} distribution is reproduced as demonstrated in Fig. 13b.

From the measured cross-section of rapidity gap events, the diffractive structure function F_2^D can be extracted. Since the scattered proton is not detected, the variable t cannot be measured and is therefore effectively integrated, although only small t contributes due to the proton form factor above. The longitudinal momentum fraction $x_{I\!P}$ can be obtained [42] from the mass M_X of the observed diffractive state through $x_{I\!P} = (Q^2 + M_X^2 - t)/(Q^2 + W^2 - m_p^2) \approx x(Q^2 + M_X^2)/Q^2$. The diffractive structure function has therefore been measured in the three variables x, Q^2 and $x_{I\!P}$. To a first approximation it was found [42] that the $x_{I\!P}$ dependence factorises and is of the form $x_{I\!P}^{-n}$ with

$n = 0.19 \pm 0.06 \pm 0.07$. This is in basic agreement with the expectation $f_{I\!P/p} \sim x_{I\!P}^{-1.16+0.5|t|}$ from the pomeron Regge trajectory above.

However, with the increased statistics and kinematic range available in the new data [55] displayed in Fig. 15, deviations from such a universal factorisation is observed. The power of the $x_{I\!P}$-dependence is found to depend on the variable $\beta = Q^2/(Q^2 + M_X^2 - t) \approx Q^2/(Q^2 + M_X^2) = z$. One way to interprete this result is by introducing a meson exchange component, e.g. $f_2^0(1270)$ expected to have x^{-n} with $n \sim 0$. With two components $x^{-n_{I\!P}}$ and x^{-n_M} one obtaines $n_{I\!P} = 1.29 \pm 0.03 \pm 0.07$ and $n_M = 0.3 \pm 0.3 \pm 0.6$ for the pomeron and meson contributions, respectively. Although the pomeron still dominates, the meson exchange contribution is here important at larger $x_{I\!P}$ and causes F_2^D to decrease slower (or $x_{I\!P} \cdot F_2^{D(3)}$ to even increase).

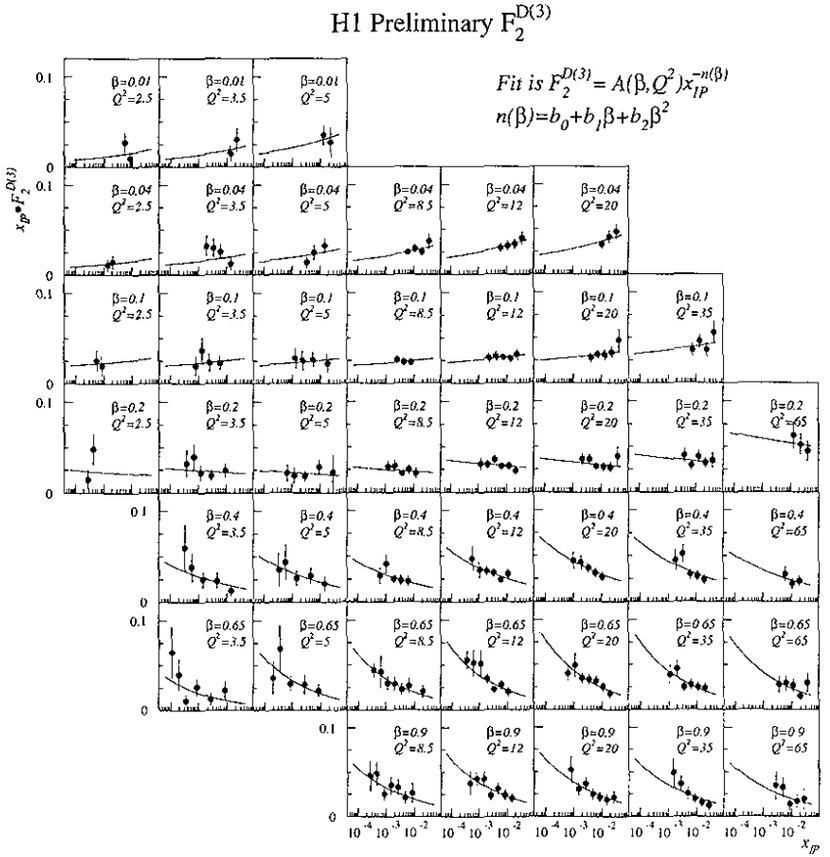

Figure 15: The diffractive structure function $x_{I\!P} \cdot F_2^{D(3)}(x_{I\!P})$ for bins in $\beta = z$ and Q^2. H1 data with fit to the form $x_{I\!P}^{-n(\beta)}$ showing factorisation breaking [55].

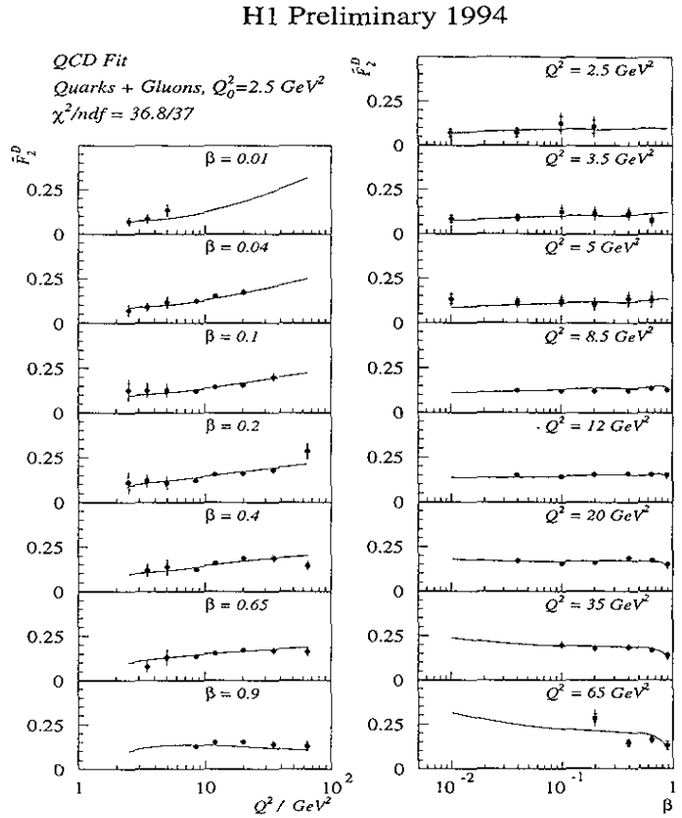

Figure 16: Data on $\tilde{F}_2^D(z = \beta, Q^2)$, i.e. the structure function of the exchanged colourless object, together with a fit of quark and gluon densities with DGLAP evolution in QCD starting at $Q_0^2 = 2.5\, GeV^2$. From [55].

By performing an integration over $x_{I\!P}$ (using data and the fitted dependence), one obtains [55] the measurement of $\tilde{F}_2^D(z = \beta, Q^2)$ shown in Fig. 16. Following the above framework, this quantity can be interpreted as the structure function of the exchanged colour singlet object, which should mainly be the pomeron. The fact that $\tilde{F}_2^D$ is essentially scale independent, i.e. almost constant with Q^2, shows that the scattering occurs on point charges. The small Q^2 dependence present is actually compatible with being logarithmic as in normal QCD evolution, although the rise with lnQ^2 persists up to large values of β in contrast to the proton structure function. Here, β can be interpreted as the momentum fraction of the parton in the pomeron, since it corresponds to Bjorken-x for the case of DIS on the pomeron. There is only a weak dependence on β such that the partons are quite hard and there is no strong decrease at large momentum fraction which is characteristic for ordinary hadrons.

These features are in accordance with a substantial gluon component in the structure of the diffractive exchange, as confirmed by a quantitative QCD analysis. Standard DGLAP evolution gives a good fit, full lines in Fig. 16, of the data on $\tilde{F}_2^D(\beta, Q^2)$. The fitted momentum distributions of quarks and gluons in the pomeron are shown in Fig. 17. Clearly, the gluon dominates and carries more than 80% of the pomeron momentum. At low Q^2 the gluon distribution is peaked at large momentum fractions, similar to the superhard component observed by UA8 [51], but becomes rather flat in β when evolved to larger Q^2.

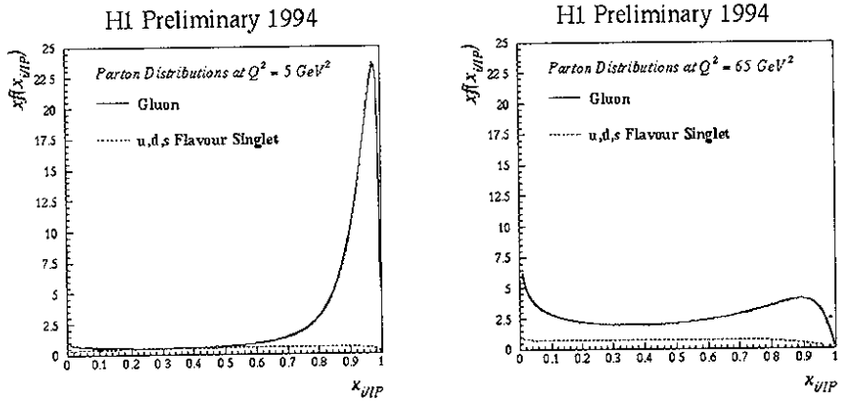

Figure 17: Momentum-weighted distributions in fractional momenta $x_{g/I\!P}$ and $x_{q/I\!P}$ of gluons and quarks (u+d+s) in the exchanged colorless object; obtained at (a) $Q^2 = 5GeV^2$ and (b) $Q^2 = 65\,GeV^2$ from a DGLAP fit to $\tilde{F}_2^D(z = \beta, Q^2)$ in Fig. 16. From [55].

Although the rapidity gap events can be reasonably well described by these phenomenological models based on pomeron exchange, there is no satisfactory understanding of the pomeron and its interaction mechanisms. On the contrary, there are conceptual and theoretical problems with this framework. The pomeron is not a real state, but can only be a virtual exchanged spacelike object. The concept of a structure function is then not well defined and, in particular, it is unclear whether a momentum sum rule should apply. In fact, the factorisation into a pomeron flux and a pomeron structure function cannot be uniquely defined [56] since only the product is an observable. It may be incorrect to consider the pomeron as being 'emitted' by the proton, having QCD evolution as a separate entity and being 'decoupled' from the proton during and after the deep inelastic scattering. Since the pomeron-proton interaction is soft, its time scale is long compared to the short space-time scale of the hard interaction. It may therefore be natural to expect soft interactions between the pomeron system and the proton both before and after the snapshot of the DIS probe. The pomeron can then not be considered as decoupled from the proton and, in particular, is part of its parton evolution in the proton.

To investigate this line of thinking, new models have recently been constructed without using the concept of a pomeron or Regge phenomenology. Instead, they are based on new ideas on soft colour interactions that give colour rearrangements which affect the hadronization.

One model [57] exploits the dominance of the photon-gluon fusion process $\gamma^* g \to q\bar{q}$ at small-x. The $q\bar{q}$ pair is produced in a colour octet state, but it is here assumed that soft interactions with the proton colour field randomizes the colour. The $q\bar{q}$ pair would then be in an octed or singlet state with probability 8/9 and 1/9, respectively. When in a singlet state, the $q\bar{q}$ pair hadronizes independently of the proton remnant, which should result in a lack of particles in between. From the photon-gluon fusion matrix element one then obtaines the diffractive structure function

$$F_2^D(x, Q^2, \xi) \simeq \frac{1}{9} \cdot \frac{\alpha_s}{2\pi} \sum_q e_q^2\, g(\xi) \cdot \beta \left\{ \left[\beta^2 + (1-\beta)^2\right] \ln \frac{Q^2}{m_g^2 \beta^2} - 2 + 6\beta(1-\beta) \right\} \quad (23)$$

The factor 1/9 is the above colour singlet probability. The following factor, including the density $g(\xi)$ of gluons with momentum fraction ξ, corresponds to the pomeron flux factor. The β-dependent factor corresponds to the pomeron structure function $\tilde{F}_2^D(\beta, Q^2)$ above, with $\beta \simeq x/\xi$ as usual. Thus, there is an effective factorisation which is similar to pomeron models. The gluon mass parameter m_g regulates the divergence in the QCD matrix element and is chosen so as to saturate the DIS cross-section at small-x with the photon-gluon fusion process. The model reproduces main features of the gap events, such as their overall rate and Q^2 dependence. However, it is simple and does not take into account higher order parton emissions and hadronization. Therefore, it cannot give as detailed predictions as the Monte Carlo models above. On the other hand, the theoretical aspects of $q\bar{q}$ pair production in the colour field of the proton has been further investigated using a semi-classical approach [58].

In the same general spirit another model has been developed independently [59, 36] using a Monte Carlo event generator approach. The starting point is the normal DIS parton interactions, with pQCD corrections in terms of matrix elements and parton showers in the initial and final state. The basic new idea is that is that there may be additional soft colour interactions (SCI) between the partons at a scale below the cut-off Q_0^2 for the perturbative treatment. Obviously, interactions will not disappear below this cut-off, the question is rather how to describe them properly. The proposed SCI mechanism can be viewed as the perturbatively produced quarks and gluons interacting softly with the colour medium of the proton as they propagate through it. This should be a natural part of the process in which 'bare' perturbative partons are 'dressed' into non-perturbative ones and the formation of the confining colour flux tube in between them. These soft interactions cannot change the momenta of the partons significantly, but they may change their colour and thereby affect the colour structure of the event. This corresponds to a modified topology of the string in the Lund model approach, as illustrated in Fig. 18.

Lacking a proper understanding on non-perturbative QCD processes a simple model was constructed to describe and simulate soft colour interactions. Treating the hard interactions in the normal way, using the LEPTO Monte Carlo [31], gives a set of partons, including the quarks in the proton remnant. Each pair of these colour charges can make a soft interaction, changing only the colour and not the momentum, which may be viewed as soft non-perturbative gluon exchange. Being a non-perturbative process, the exchange probability cannot be calculated and is therefore described by a phenomenological parameter R. The number of soft exchanges will vary event-by-event and change the colour topology such that, in some cases, colour singlet subsystems arise separated in rapidity as shown in Fig. 18bc. Here, (b) can be seen as a switch of anticolour between the antiquark and the diquark and (c) as a switch of colour between the two quarks. Colour exchange

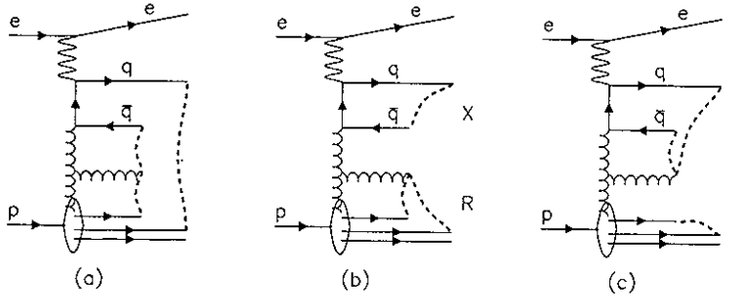

Figure 18: The string configuration in a gluon-induced DIS events in (a) conventional Lund string model connection of partons, and (b,c) after string reconnection due to soft colour interactions.

between the perturbatively produced partons and the partons in the proton remnant are of particular importance for the gap formation.

Both gap and non-gap events arise such that the model attempts to give a general description of DIS. In fact, it can give a fair account [36] for such 'orthogonal' observables as rapidity gaps and the large forward $E_\perp$ flow discussed in section 5. The rate and main properties of the gap events are qualitatively reproduced, e.g. the η_{max} distribution in Fig. 13b. The gap rate depend on the parameter R, but the dependence is not strong giving a stable model with $R \simeq 0.2$–0.5. The gap events show properties characteristic of diffraction as demonstrated in Fig. 19. Here, $t = (p_p - p_R)^2$ is the momentum transfer from the incoming proton to the emerging R-system. The exponential dependence arises in the model from the gaussian intrinsic transverse momentum (Fermi motion) of the interacting parton which is balanced by the proton remnant system, i.e. $exp(-k_\perp^2/\sigma_i)$ with $\sigma_i \simeq 0.4\,GeV$ and $t \simeq -k_\perp^2$. The forward R-system (Fig. 19b) is dominantly a single proton, as in a diffractive scattering, but there is also a tail corresponding to proton dissociation. The longitudinal momentum spectrum of protons in Fig. 19c shows a clear peak at large fractional momentum x_L. Defining events having a leading proton with $x_L > 0.95$ as 'diffractive', one observes in Fig. 19bc that most of these events fulfill the gap requirement.

One may ask whether this kind of soft colour interaction model is essentially a model for the pomeron. This should not be the case as long as no pomeron or Regge dynamics is introduced. At present, the model has only one new free parameter, the colour exchange probability R. Other parameters belong to the conventional DIS model [31] and have their usual values. The rate and size of gaps do, however, depend on the amount of parton emission. In particular, more initial state parton shower emissions will tend to populate the forward rapidity region and prevent gap formation. It is therefore interesting to note that te DGLAP-based LEPTO gives about the correct rate of gap events, whereas ARIADNE with its more abundant CDM-based radiation gives a too low gap event rate. It is therefore important to consider the theoretical foundations for the parton shower models. The DGLAP scheme is developed for the inclusive case, i.e. for F_2 corresponding to summing ladder diagrams. However, an exclusive parton final state corresponds to a cut

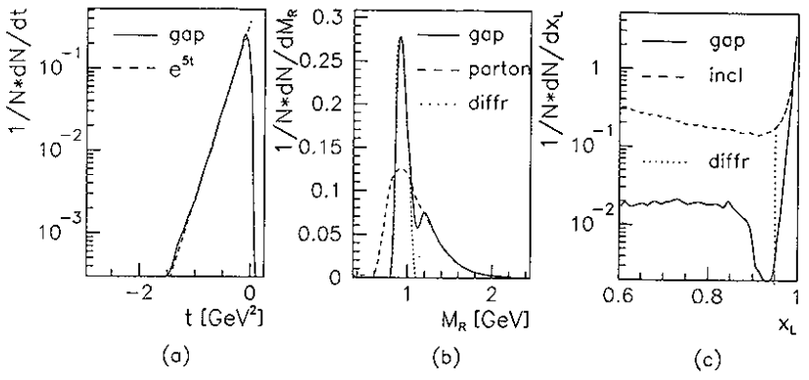

Figure 19: Squared momentum transfer t from initial proton to remnant system R for 'gap' events compared with the exponential slope $1/\sigma_i^2 = 5\,GeV^2$. (b) Invariant mass M_R of the forward remnant system for 'gap' events at the hadron level (solid line) and parton level (dashed line) compared with 'diffractive' events at the hadron level (dotted line). (c) Longitudinal momentum fraction x_L for final protons in 'gap' events (solid line), all events (dashed line) and 'diffractive' events (dotted line). From [36]

through the ladder as illustrated in Fig. 7a. It is then not fully clear that DGLAP (or other evolution equations) are directly applicable to account for all configurations. The mean behaviour of emissions is probably well described, but not necessarily the fluctuations. Considering evolution paths event-by-event in the $ln\,k_\perp^2$—y phase space of emitted partons (Fig. 11), 'downwards' fluctuations will favour rapidity gaps and 'upwards' fluctuations produce a larger forward $E_\perp$ flow. Thus, even with an increased mean parton emission, the gap rate may be large enough provided that the fluctuations are sufficient.

It should be noted that other types of soft interactions have been discussed in other contexts. Colour reconnections causing modified Lund string topology has been investigated [60] in case of $e^+e^- \to W^+W^- \to q_1\bar{q}_2q_3\bar{q}_4$, where the two resulting strings may interact. Soft interactions of a colour charge moving through a colour medium has been considered [61] and argued to give rise to large K-factors in Drell-Yan processes and synchrotron radiation from the QCD vacuum. Although these studies are not related to rapidity gaps, they contribute to a more general attempt to understand non-perturbative QCD.

7 Conclusions

In this review of HERA physics we have concentrated on manifestations of QCD parton dynamics at small-x. HERA has discovered a large increase of the structure function F_2 at small-x, corresponding to an increase of the parton densities in the proton. Present data can be described by conventional DGLAP evolution and seem to follow the double asymptotic scaling characteristic for large $log\,Q^2$ and $log\,1/x$. Novel QCD dynamics, such as embodied in the BFKL and GLR equations, may however be present at some level. To explore this one needs either still smaller x or other observables. The latter is provided by the hadronic final state, which reflects the properties of the underlying parton emissions. Forward transverse energy flows have been investigated in detail, but giving an inconclusive result. Recent studies of high-$p_\perp$ particle spectra and forward jet cross-sections do, however, give some evidence for the predicted BFKL behaviour.

The discovery of rapidity gaps events has given the first measurement of diffractive deep inelastic scattering and, in particular, the diffractive structure function. The observations can be well described by models based on pomeron exchange in Regge phenomenology, which gives a direct measure of the parton structure of the pomeron. In this framework, the pomeron is found to be dominated by a hard gluon component, which evolves through QCD to a give an observable quark density which has a rather flat momentum distribution.

The theoretical problems with the pomeron concept has motivated the development of new, non-pomeron models which introduce novel soft colour interaction mechanisms. Here, partons interact with the 'background' colour field of the proton remnant system in such a way to produce colour singlet systems that are separated in rapidity. These models describe the salient features of the data and provide an interesting alternative that may provide a better way to understand the diffractive interaction mechanism.

HERA also provides a rich field for many other physics topics, only some of which were discussed above. Much is already available, e.g. on electroweak physics, jets and α_s measurements, heavy flavour production, photoproduction etc. In the coming years, more data giving higher statistics and larger kinematical coverage will give more results, in particular concerning rare processes at large Q^2, where deviations from the standard model may occur.

Acknowledgments

I am grateful to prof. Nachtmann and the other organizers for a very interesting and pleasant meeting in Heidelberg.

References

[1] R. Hofstadter, R.W. McAllister, Phys. Rev. 98 (1954) 217

[2] M. Breidenbach et al., Phys. Rev. Lett. 23 (1969) 935

[3] F. Eisele, Rep. Progr. Phys. 49 (1986) 233
M. Diemoz, F. Ferroni, E. Longo, Phys. Rep. 130 (1986) 293
T.Sloan, G. Smadja, R. Voss, Phys. Rep. 162 (1988) 45

[4] F.E. Close, 'An Introduction to Quarks and Partons', Academic Press, London 1980

[5] G. Ingelman et al., in [7], Vol. 1, p. 3

[6] M. Bengtsson, G. Ingelman, T. Sjöstrand, in [7], Vol. 1, p. 149

[7] Proceedings HERA Workshop 1987, Ed. R.D. Peccei, DESY 1988

[8] Proceedings 'Physics at HERA', Eds. W. Buchmueller, G. Ingelman, DESY 1992

[9] Proceedings 'Future Physics at HERA', Eds. G. Ingelman, A. De Roeck, R. Klanner, DESY 96-235, Hamburg 1996

[10] ZEUS collaboration, M. Derrick et al., Phys. Rev. Lett. 75 (1995) 1006
H1 collaboration, S. Aid et al., Phys. Lett. B379 (1996) 319

[11] H1 collaboration, S. Aid et al., Nucl. Phys. B470 (1996) 3

[12] ZEUS collaboration, M. Derrick et al., Z. Phys. C72 (1996) 399

[13] G. Altarelli, G. Parisi, Nucl. Phys. B126 (1977) 298
V.N. Gribov, L.N. Lipatov, Sov. J. Nucl. Phys. 15 (1972) 438
Yu. Dokshitzer, Sov. Phys. JETP 46 (1977) 641

[14] B. Badelek et al., J. Phys. G: Nucl. Part. Phys. 22 (1996) 815

[15] E.A. Kuraev, L.N. Lipatov, V.S. Fadin, Sov. Phys. JETP 45 (1977) 199
Y.Y. Balitsky, L.N. Lipatov, Sov. J. Nucl. Phys. 28 (1978) 822

[16] M. Ciafalone, Nucl. Phys. B296 (1988) 49
S. Catani, F. Fiorani, G. Marchesini, Phys. Lett. B234 (1990) 339; Nucl. Phys. B336 (1990) 18

[17] H1 collaboration, C. Adloff et al., DESY 96-236

[18] A.D. Martin, W.J. Stirling, R.G. Roberts, Phys. Lett. B354 (1995) 155

[19] CTEQ collaboration, J. Botts et al., Phys. Lett. B304 (1993) 159

[20] M. Glück, E. Reya, A. Vogt, Z. Phys. C67 (1995) 433

[21] R.D. Ball, S. Forte, Phys. Lett. B335 (1994) 77

[22] W. Buchmüller, D. Haidt, DESY 96-061

[23] L.V. Gribov, E.M. Levin, M.G. Ryskin, Phys. Rep. 100 (1983) 1

[24] A.H. Mueller, J. Qiu, Nucl. Phys. B268 (1986) 427

[25] J. Kwiecinski et al., Phys. Rev. D42 (1990) 3645
J. Bartels, J. Blümlein, G.A. Schuler, Z. Phys. C50 (1991) 91

[26] E.M. Levin, M.G. Ryskin, Nucl. Phys. B(Proc. Suppl.) 18C (1990) 92
A. Mueller, Nucl. Phys. B (Proc. Suppl.) 18C (1990) 125

[27] M. Froissart, Phys. Rev. 123 (1961) 1053

[28] ZEUS collaboration, paper pa02-025 at ICHEP'96, Warsaw 1996

[29] A. Donnachie, P.V. Landshoff, Z. Phys. C61 (1994) 139

[30] H1 collaboration, Z. Phys. C63 (1994) 377; Phys. Lett. B356 (1995) 118

[31] G. Ingelman, A. Edin, J. Rathsman, LEPTO 6.5, DESY 96-057, Comput. Phys. Commun. in press

[32] B. Andersson et al., Phys. Rep. 97 (1983) 31

[33] K. Golec-Biernat et al., Phys. Lett. B335 (1994) 220
J. Kwieciński et al., Phys. Rev. D50 (1994) 217

[34] L. Lönnblad, ARIADNE version 4, Comp. Phys. Comm. 71 (1992) 15

[35] B. Andersson et al., Z. Phys. C43 (1989) 621

[36] A. Edin, G. Ingelman, J. Rathsman, DESY 96-060, Z. Phys. C74 in press

[37] M. Kuhlen, Phys. Lett. B382 (1996) 441

[38] H1 collaboration, C. Adloff et al., DESY 96-215

[39] H1 collaboration, paper pa03-049 at ICHEP'96, Warsaw 1996

[40] J. Bartels, A. De Roeck, M. Loewe, Z. Phys. C54 (1992) 635

[41] ZEUS collaboration, M. Derrick et al., Phys. Lett. B315 (1993) 481;
Z. Phys. C68 (1995) 569

[42] H1 coll., Nucl. Phys. B429 (1994) 477; Phys. Lett. B348 (1995) 681

[43] ZEUS collaboration, private communication

[44] G. Ingelman, P.E. Schlein, Phys. Lett. B152 (1985) 256

[45] K. Goulianos, Phys. Rep. 101 (1983) 169

[46] F.E. Low, Phys. Rev. D12 (1975) 163
S. Nussinov, Phys. Rev. Lett. 34 (1975) 1286; Phys. Rev. D14 (1976) 246

[47] Yu. A. Simonov, Phys. Lett. B249 (1990) 514; Nucl. Phys. B (Proc. Suppl.) 23 (1991) 283

[48] WA91 collaboration, Phys. Lett. B324 (1994)509; B353 (1995) 589

[49] A. Donnachie, P.V. Landshoff, Phys. Lett. B191 (1987) 309; Nucl. Phys. B303 (1988) 634

[50] UA8 collaboration, R. Bonino et al., Phys. Lett. B211 (1988) 239

[51] UA8 collaboration, A. Brandt et al., Phys. Lett. B297 (1992) 417

[52] G. Ingelman, K. Prytz, Z. Phys. C58 (1993) 285

[53] P. Pruni, G. Ingelman, Phys. Lett. B311 (1993) 317
P. Bruni, A. Edin, G. Ingelman, POMPYT 2.6

[54] H. Jung, Comp. Phys. Commun. 86 (1995) 147

[55] H1 collaboration, paper pa02-061 at ICHEP'96, Warsaw 1996

[56] P.V. Landshoff, *in* Workshop on DIS and QCD, Paris 1995, Eds. J.F. Laporte, Y. Sirois, p. 371

[57] W. Buchmüller, A. Hebecker, Phys. Lett. B355 (1995) 573

[58] W. Buchmüller, A. Hebecker, Nucl. Phys. B476 (1996) 203

[59] A. Edin, G. Ingelman, J. Rathsman, Phys. Lett. B366 (1996) 371

[60] G. Gustafson, U. Pettersson, P. Zerwas, Phys. Lett. B209 (1988) 90
T. Sjöstrand, V. Khoze, Z. Phys. C62 (1994) 281
G. Gustafson, J. Häkkinen, Z. Phys. C64 (1994) 659

[61] O. Nachtmann, A. Reiter, Z. Phys. C24 (1984) 283
G.W. Botz, P. Heberl, O. Nachtmann, Z. Phys. C67 (1995) 143